Water Research 238 (2023) 119990



Contents lists available at ScienceDirect

Water Research

journal homepage: www.elsevier.com/locate/watres

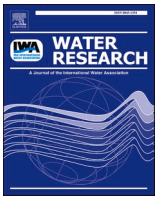



Structure and composition of natural ferrihydrite nano-colloids in anoxic groundwater

Maya Engel [a], Vincent Noël [a], Samuel Pierce [a], Libor Kovarik [b], Ravi K. Kukkadapu [b], Juan S. Lezama Pacheco [c], Odeta Qafoku [b], J. Ray Runyon [d], Jon Chorover [d], Weijiang Zhou [e], John Cliff [b], Kristin Boye [a], John R. Bargar [b,*]

[a] Environmental Geochemistry Group, SLAC National Accelerator Laboratory, Menlo Park, CA 94025, USA
[b] Environmental Molecular Sciences Laboratory, Pacific Northwest National Laboratory, Richland, WA 99354, USA
[c] Department of Earth System Science, Stanford University, Stanford, CA 94305, USA
[d] Department of Environmental Science, University of Arizona, Tucson, AZ 85721, USA
[e] Division of CryoEM and Bioimaging, SSRL, SLAC National Accelerator Laboratory, Menlo Park, CA 94025, USA

ARTICLE INFO

Keywords:
Fe mineral
Oxidation–reduction
Electron microscopy
EXAFS
Mössbauer spectroscopy

ABSTRACT

Fe-rich mobile colloids play vital yet poorly understood roles in the biogeochemical cycling of Fe in groundwater by influencing organic matter (OM) preservation and fluxes of Fe, OM, and other essential (micro-)nutrients. Yet, few studies have provided molecular detail on the structures and compositions of Fe-rich mobile colloids and factors controlling their persistence in natural groundwater. Here, we provide comprehensive new information on the sizes, molecular structures, and compositions of Fe-rich mobile colloids that accounted for up to 72% of aqueous Fe in anoxic groundwater from a redox-active floodplain. The mobile colloids are multi-phase assemblages consisting of Si-coated ferrihydrite nanoparticles and Fe(II)-OM complexes. Ferrihydrite nanoparticles persisted under both oxic and anoxic conditions, which we attribute to passivation by Si and OM. These findings suggest that mobile Fe-rich colloids generated in floodplains can persist during transport through redox-variable soils and could be discharged to surface waters. These results shed new light on their potential to transport Fe, OM, and nutrients across terrestrial-aquatic interfaces.

1. Introduction

Fe-rich mobile colloids are believed to play vital roles in (micro-) nutrient biogeochemical cycling in natural waters (Boye et al., 2010; Homoky et al., 2021) because they strongly adsorb and transport organic matter (OM) and moderate the bioavailability of P, Fe, Mn, and other metals (Liao et al., 2020; Thompson et al., 2006; Yan et al., 2016; Löv et al., 2018; Henderson et al., 2012; Liao et al., 2017; Pokrovsky and Schott, 2002; Mylon et al., 2004). Recent in-stream studies suggest that Fe-OM colloids originating in soils are important sources of riverine Fe (Olshansky et al., 2018), indicating that soil-stream interfaces are important loci of watershed Fe export. Yet, our ability to model colloid chemistry and transport across terrestrial-aquatic interfaces is poor, due to a dearth of information on mobile colloid phase identity and stability in natural aquatic systems. Fe is relatively abundant in floodplains, where spatially/temporally alternating soil redox conditions are favorable to the formation of nano-scale Fe oxides and sulfides (Pokrovsky and Schott, 2002; Olshansky et al., 2018; Liao et al., 2016; He et al., 2019; Noël et al., 2020). These nanophases undergo rapid reductive or oxidative dissolution. For them to transport across floodplains and stream water, *i.e.*, across oxic and anoxic environments, continuous localized formation or dissolution of these nanophases must co-occur, or they need to be chemically/kinetically stabilized against redox-driven dissolution. Complexation or co-precipitation of Fe nanominerals with OM (Noël et al., 2020; Thomasarrigo et al., 2020; Sharma et al., 2010) or with dissolved cations/anions can significantly alter these dynamics by stabilizing the nanophase (Schulz et al., 2022; Kaegi et al., 2010). The role of organic and inorganic impurities in Fe-colloid structure and composition is key to understanding colloid mobility and persistence.

Groundwater mixing at subsurface interfaces promotes contact between oxic and reducing (often sulfidic) soil porewaters that can

* Corresponding author.
E-mail address: john.bargar@pnnl.gov (J.R. Bargar).

https://doi.org/10.1016/j.watres.2023.119990
Received 11 February 2023; Received in revised form 19 April 2023; Accepted 20 April 2023
Available online 22 April 2023
0043-1354/© 2023 Published by Elsevier Ltd.

generate either ferrihydrite and/or FeS colloids (Noël et al., 2020; Jakobsen and Postma, 1999; Hassellöv and von der Kammer, 2008), as well as Fe mineral transformation products such as lepidocrocite, goethite, and magnetite (Schulz et al., 2022; Qafoku et al., 2020; Thompson et al., 2006). Laboratory based studies have found that the transformation of ferrihydrite to FeS depends on the S(-II)-to-Fe molar ratio, as well as on the presence and functional group content of OM (Noël et al., 2020; Thomasarrigo et al., 2019), whereas transformation of ferrihydrite to crystalline Fe oxyhydroxides is dependent on Fe(II)/Fe (III) aqueous molar ratio and the type of inorganic ligands in solution (Cl^-, SO_4^{2-}, CO_3^{2-}) (Qafoku et al., 2020; Hansel et al., 2005; Cornell and Giovanoli, 1985). In contrast, OM coatings have been shown to prolong the stability of ferrihydrite colloid nanoparticles in solution (Noël et al., 2020; Thomasarrigo et al., 2020; Sharma et al., 2010). The presence of strongly adsorbed ions such as SiO_4^{4-}, PO_4^{3-}, and even Ca^{2+} can also moderate the chemical stability of Fe colloids (Kaegi et al., 2010; Lapworth et al., 2013; Moens et al., 2021; Stolpe et al., 2013) – although the influence of SiO_4^{4-} loading on transformations of ferrihydrite triggered by Fe(II) has remained controversial as both strong and minimal effects have been reported (Schulz et al., 2022; Jones et al., 2009; Kukkadapu et al., 2004).

The majority of studies on Fe-nanophases have been performed using either laboratory-synthesized colloids (Liao et al., 2020; Liao et al., 2017; Li et al., 2019) or fines extracted from soils/sediments (Rod et al., 2020; Xia et al., 2018); thus, they are not necessarily representative of mobile groundwater colloids, which are expected to exhibit pronounced compositional complexity. Our objective here was to isolate naturally occurring, mobile Fe-rich colloids from soil water and characterize them at nano- and molecular-scale detail to understand their persistence and impacts on Fe and nutrient transport.

Soil water samples were collected from riparian anoxic zones of a redox-active floodplain that is proximal to the Slate River (Crested Butte, CO, USA) across the hydrological transition from snowmelt to baseflow conditions. This system serves as a model for the numerous similar gravel bed river-floodplain systems in the Rocky Mountains and other Alpine environments across the globe. A suite of advanced methodologies was utilized to characterize mobile colloids collected during snowmelt, including cascade filtration, asymmetric flow field flow fractionation (AF4), extended X-ray absorption fine structure spectroscopy (EXAFS), Mössbauer spectroscopy, nanoscale secondary ion mass spectrometry (NanoSIMS), cryo transmission electron microscopy (cryo-TEM), and transmission and scanning electron microscopies (TEM/SEM) coupled with energy dispersive X-ray spectroscopy (EDS). This comprehensive approach identified mobile ferrihydrite-based nanoparticles in reducing waters. The colloids were identified as multi-phase nanoparticles comprised of ferrihydrite coated by Si and OM that is further associated with Fe(II) and Fe(III). The stability of the ferrihydrite phase is attributed to the passivating effect of the Si coating and OM matrix that ultimately encapsulate the ferrihydrite nanoparticles. The colloids exhibited a seasonally variable composition, with a lower contribution of Fe(II) under more oxic baseflow conditions. This study provides novel insights of the nanoscale structure and composition of natural Fe-rich colloids, with implications for OM and essential element as well as contaminant transport in watersheds.

2. Materials and methods

2.1. Site description and sample collection

Here, we refer to colloids as nanoclusters/complexes/particles etc. in the 20–220 nm size range. Therefore, colloid concentrations were quantified as the difference between measured analyte concentrations of the 0.22 and 0.02 μm filtrates. Porewater samples were collected from a floodplain along the upper Slate River (Crested Butte, CO; 38°54′34.59″ N, 107°1′43.40″ W) in May–July of 2021 using a network of installed Rhizon™ soil moisture samplers (0.6 μm pore size, 19.60.21F, Rhizosphere Research Products) at depths of 130 to 180 cm. Rhizons were modified to connect to surface sampling ports with aluminum (instead of plastic) tubing to minimize oxygen intrusion along the sampling lines. Samples were extracted using valved syringes and immediately injected through a 0.22 μm, 0.1 μm (25 mm, PES, Sartorius) or 0.02 μm filter (25 mm, Anatop, Whatman) into N_2-purged, glass serum vials having thick rubber stoppers to preserve redox conditions. Samples were shaded from sun exposure during extraction from the subsurface, stored and shipped on ice in the dark, and then preserved at 4 °C in the dark in the laboratory prior to analysis (aqueous phase chemistry measurements and advanced characterizations were performed within days and several weeks of sampling, respectively).

2.2. Sample characterization

Aliquots were removed from the serum vials in an anoxic chamber to prevent exposure to oxygen. Ferrous iron concentrations were measured using the ferrozine method (Viollier et al., 2000; Stookey, 1970) on a plate reader (800TS, BioTek) while total Fe, as well as Ca were measured using an inductively coupled plasma optical emission spectrometer (ICP-OES; iCAP 6300, Thermo Scientific, Cambridge, U.K.). Fe(III) levels were calculated as the difference between total Fe to Fe(II) concentrations. Dissolved organic carbon concentrations were quantified on a total organic carbon (TOC) analyzer (TOC-L, Shimadzu, Kyoto, Japan).

2.3. Cryo-transmission electron microscopy

Porewater solution (130 or 180 cm depth; 0.22, 0.1, and 0.02 μm; sampled in May and June 2021) was blotted (3 μL) onto a Quantifoil holey carbon TEM grid (R 2/1 with 2 nm carbon film) and immediately plunged into liquid ethane using a Thermo fisher Vitrobot. The frozen grids were maintained under liquid nitrogen until transfer to the cryo-TEM. Experiments were performed on a Thermo Fisher Titan Krios G3 TEM operated at 300 kV located at the Stanford-SLAC Cryo-EM center (S^2C^2). Cryo-TEM images were acquired by a Gatan K3 direct-detection camera in energy filtered electron-counting mode with the Dose-Fractionation function. The images were taken at a nominal magnification of 215,000 with a pixel size of 0.41 Å by 0.41 Å and electron dose rate of 45 $e^-/Å^2$ /s per image. The exposure time was 2s per image with 0.1s per frame, resulting in 20 frames per image. The targeting defocus was set between 500 to 1 μm to ensure sufficient contrast of the colloid particles without losing high-resolution details. The motion-corrected images were then used to analyze the morphology of the colloids.

2.4. Transmission electron microscopy

Colloids from the porewater solution (180 cm depth; 0.22 and 0.1 μm; sampled in May–July 2021) were deposited on a lacey carbon Cu grid (300 mesh) inside an anoxic chamber. Samples were transferred to the TEM under anoxic conditions using a Fischione vacuum transfer holder (Model 2560). Microstructural observations were performed with a Thermo Fisher Scientific Themis Z 30–300 STEM operated at 60 kV. The images were collected in both conventional bright field imaging mode using a CMOS Ceta camera and scanning mode with a high-angle annular dark-field (HAADF) detector. Energy-dispersive X-ray spectroscopy was performed with a Super-X G2 detector. Acquisitions were made with probe currents in the range of 50–80 pA for the different samples analyzed. All maps were obtained with multi-frame drift corrected acquisition. EDS data processing was performed with Velox software from Thermo Fisher Scientific. Scanning electron microscopy was performed to validate the TEM results – details are presented in the Supporting Information (Page S12).

2.5. Mössbauer spectroscopy

Colloids were collected on a 1 to 3 nm filter membrane (47 mm, PES,

Ultracel) by filtering *ca* 0.5 L of porewater solution (from 130 to 180 cm depth; <0.22 μm; sampled in Sep 2021) in an anoxic chamber. Mössbauer spectra of the filtered material (handled in an anoxic chamber) were collected at multiple temperatures (298 K, 225 K, 77 K, 12 K, and 5 K - only the 5 K spectrum is shown) to identify Fe mineral composition. Data were collected at the Environmental Molecular Science Laboratory (EMSL), WA, USA, using a Web Research Company (St. Paul, MN) instrument that included a closed-cycle cryostat (SHI-850, Janis Research Company, Inc., Wilmington, MA), a Sumitomo CKW-21 He compressor unit (Allentown, Pennsylvania), and a Ritverc NaI detection system (St. Petersburg, Russia). A ^{57}Co/Rh source was used as the gamma energy source. Data acquisition and data processing followed previously reported procedures (Peretyazhko et al., 2012), see Supporting Information for more details (Page S5).

2.6. Fe X-ray absorption spectroscopy

Fe K-edge X-ray absorption near edge structure (XANES) and extended X-ray absorption fine structure (EXAFS) spectra of the porewater solutions, filtered at 0.22 μm, were collected at 10 K (liquid He cryostat). These spectra were collected in fluorescence mode using a 30-element germanium detector at beamline 7–3, at the Stanford Synchrotron Radiation Lightsource (SSRL). Samples were prepared in an anoxic chamber. The porewater solution was mixed with glycerol (3:1 ratio) to avoid ice crystallization at 10 K, and the mixture was loaded into a plastic holder which was sealed with Kapton® tape. The holder was mounted on a cryostat sample rod and brought to the beamline in a liquid nitrogen bath before being rapidly transferred into the liquid He cryostat. The Si(220) double crystal monochromator was detuned by 50% to minimize higher order harmonics and the beam energy was calibrated by setting the first K-edge inflection point of a Fe foil to 7112 eV (double transmission mode). For each sample, 16 to 24 scans were recorded, and the spectra were subsequently inspected for beam-damage (none detected), averaged, normalized, and the background subtracted from the normalized data using the ATHENA software (Ravel and Newville, 2005). Fe K-edge EXAFS spectra were analyzed by LC-LS fitting using experimental Fe K-edge EXAFS spectra from natural and synthetic model compounds from a large dataset of references compounds (>30; Table S6) that was narrowed down based on PCA analysis (no of significant components) and results from the TEM and Mössbauer analyses (plausible components). LC-LS fits were performed using the ATHENA software. Linear coefficients were constrained to be only positive. The accuracy of this fitting procedure ranges between ± 25% and ± 5% of the stated values for each individual contribution and the detection limit for minor species is estimated to be ≥10% (Ostergren et al., 1999; Cancès et al., 2005). Additionally, the Fe K-edge EXAFS spectra were analyzed by shell-by-shell fitting, using the ARTEMIS software with FEFF code 6 (Ankudinov and Ravel, 1998). Backscattering phase and amplitude functions were calculated using the FEFF6 program for Fe(III)-C, Fe(II)-C, Fe(III)-O, Fe(II)-O, Fe(III)-S, Fe(II)-S, Fe(III)-Fe (III), Fe(III)-Fe(II), and Fe(II)-Fe(II) pairs. The fixed amplitude reduction factor, $S0_2$, was fixed at 0.83 for all samples (Liu and Hesterberg, 2011). Fits were performed in R-space over a 1–4 Å range, and all paths are single scattering. Only interatomic distances with acceptable uncertainty values were used in the final fit. The quality of the LC-LS and shell-by-shell fits was estimated by an R-factor parameter (Rf) of the following form: $Rf=\Sigma(k^3\chi_{exp}- k^3\chi_{fit})^2/ \Sigma(k^3\chi_{exp})^2$.

2.7. Additional characterization

Nanoscale Secondary Ion Mass Spectrometry (NanoSIMS) was employed to visualize the elemental distribution of stable isotopes in a representative colloid sample. In brief, colloids were deposited on a Cu-grid and dried, after which SEM was used to locate the colloids prior to the NanoSIMS analysis. In addition, asymmetrical flow field flow fractionation combined with UV, multiangle light scattering and differential refractive index detection (AF4-UV-MALS-dRI) was used to characterize the colloids with respect to root mean square radius (r_{rms}), hydrodynamic radius (r_h), and shape factor (r_{rms}/r_h) distributions (Trostle et al., 2016). A detailed description of the NanoSIMS and AF4 analyses are presented in the Supporting Information (Pages S9–10 and S14).

3. Results

3.1. Colloid abundance, size, and nanoscale elemental distributions

Colloids collected during snowmelt (high river stage, saturated soils, May–June), referred to as "snowmelt colloids", were measured using a comprehensive suite of methods (Table S1). Colloids collected under baseflow drought conditions (late July), referred to as "baseflow colloids", were measured with EXAFS (common to both time points) and Mössbauer spectroscopy. Here we summarize our findings in a method-by-method order. Fe colloid concentrations (>0.02 μm fraction), as well as the distribution of Fe(II) and Fe(III) within the colloids varied substantially from May to July of 2021 (Table S2), despite comparable total aqueous Fe concentrations (<0.22 μm). Fe-rich colloid concentrations peaked during snowmelt (late May through mid-June) and then decreased as baseflow conditions were reached in July. Fe(II) in the colloidal fraction followed a similar trend, with a large drop in July (11% of total Fe) as compared to May (39%). Colloidal Fe(II) concentrations were inversely related to dissolved oxygen levels in July (Table S2), which rose from an average of 0.08 mg L^{-1} in June to 0.35 mg L^{-1} in July (approx. 0.9% and 3.9% of O_2 saturation), as soils drained during seasonal summer drying (Dewey et al., 2021).

Cryo-TEM imaging of the snowmelt colloids revealed spherical particles ranging in size from approximately 10 to 100 nm (Fig. 1). These included mono-dispersed spheres, as well as elongated assemblages of spheroids. The fact that the colloidal nano-spheres withstood radiation damage testing is consistent with a dominantly inorganic composition of the colloids (Fig. S1). AF4 analysis also indicated a heterogeneous particle size distribution, with a root mean square radius, r_{rms}, in the 10 to 200 nm range (Fig. S2). Furthermore, the ratio of root mean square radius to the hydrodynamic radius (r_{rms}/r_h), commonly known as the shape factor, ranged from approximately 0.4 to 1.2, further supporting cryo-TEM imaging results showing the presences of spherical particles and spheroid assemblages of varying shapes. (Trostle et al., 2016).

TEM- and SEM-EDS elemental mapping of the snowmelt colloids (Figs. 2 and S3) identified Fe (13.3 atom%), O (42.8%), C (36.4%), and Si (6.7%) as the primary constituents. Smaller contributions from Ca (0.38%), Al (0.31%), and S (0.03%) were also present. Calculated solid-phase molar ratios were O/Fe=11.3, C/Fe=12.8, and Si/Fe=1.0. These results are consistent with a mixture of Fe-oxide minerals and OM. Aluminosilicates appear to be absent based on the large disparity in abundance between Si/Al (20:1). Rather, the equimolar ratio of Fe and Si suggests that Si is adsorbed on (as monomers or polymers) or coprecipitated in the colloids. Moreover, the elemental map overlay of Fe, Si and C (Fig. 2) suggests that the Fe particles are coated by Si and embedded in an OM-Si matrix (Adusei-Gyamfi et al., 2019). Nano-SIMS analysis confirmed the co-occurrence of Fe, O, Si, C, N, and S (Figs. S4–5). Co-location of Fe and O supports the presence of an Fe-oxide mineral, and co-locality of C and N implies contribution from N-rich OM (*e.g.*, proteins and nucleic acids) (Fig. S4). Some domains within examined samples exhibited spatial association between Fe and low-abundance S (Fig. S5), suggesting that Fe–S interactions may be present at low abundance (more details in Supporting Information Page S14).

3.2. Colloid phase identity

TEM selected-area electron diffraction (SAED) analysis (Fig. 2) of snowmelt colloid samples shows two weak diffraction rings corresponding to ɒ-spacing values of 0.146 and 0.251 nm, that are consistent

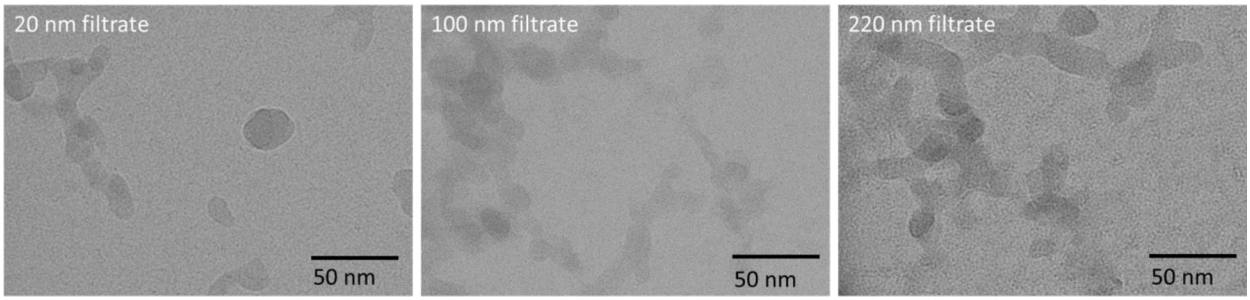

Fig 1. Representative cryo-transmission electron microscopy (cryo-TEM) images of Fe-rich colloids collected at 130 or 180 cm depth during snowmelt of 2021. Left panel: flash-frozen filtrate after passing through a 20 nm membrane (130 cm; May 24); Middle panel: 100 nm filtrate (130 cm; May 24); Right panel: 220 nm filtrate (180 cm; June 15).

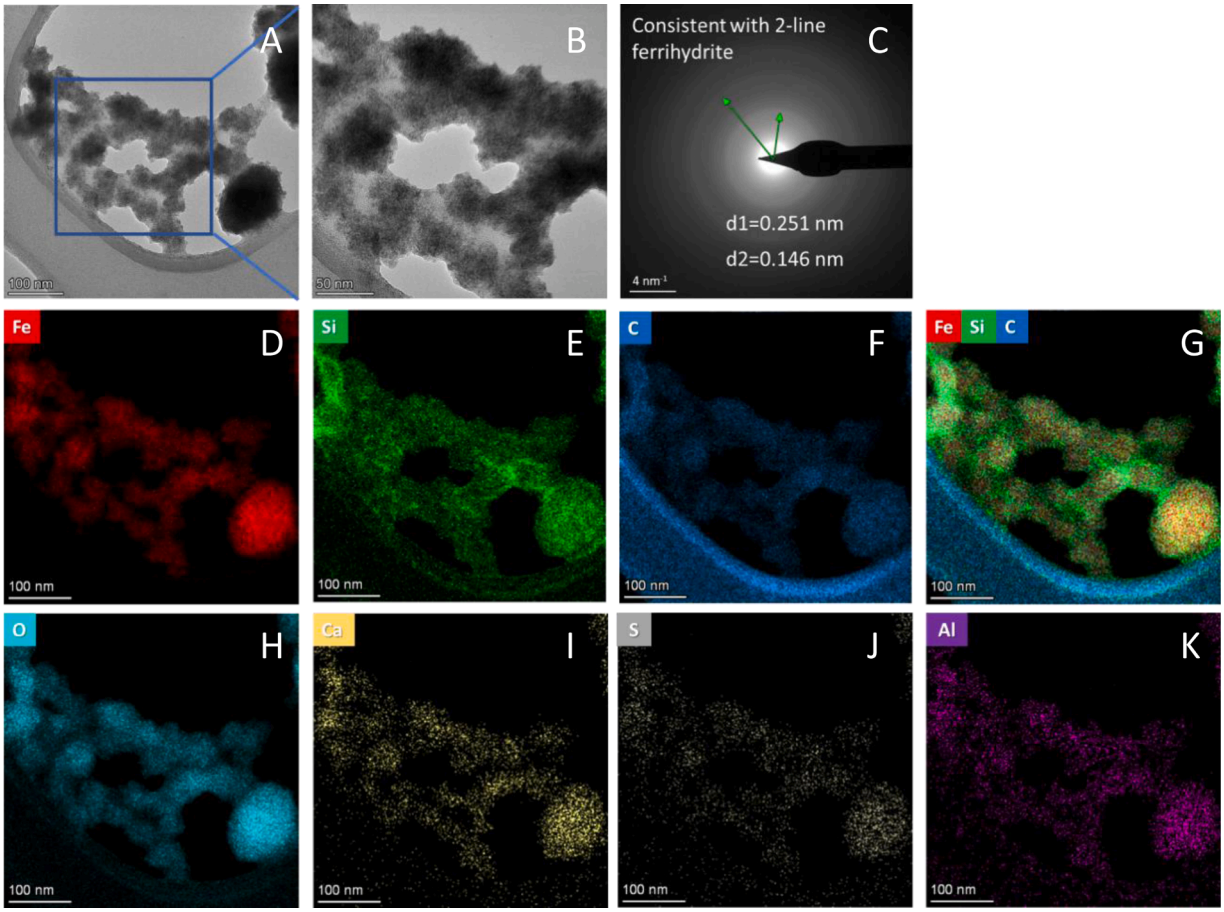

Fig 2. Representative transmission electron microscopy (TEM) images and corresponding energy dispersive X-ray spectroscopy (EDS) maps of Fe-rich colloids collected at 180 cm depth during snowmelt (May 24) of 2021. Top row: Sample morphology (Panels A and B) and diffraction rings (C) are consistent with 2-line ferrihydrite; Middle row, maps in panels D-F correspond to Fe, Si and C, respectively. Panel G: tricolor map of Fe, Si, and C; Bottom row: Panels H-K are maps of O, Ca, S and Al.

with a poorly crystalline 2-line ferrihydrite (Janney et al., 2000; Dardenne et al., 2002). Mössbauer spectroscopy of a baseflow colloid sample confirmed a best fit with two ferrihydrite phases containing different OM/Si ratios (Chen et al., 2015; Eusterhues et al., 2008; Murad and Cashion, 2004). Goethite, hematite, magnetite, lepidocrocite, and FeS, were not detected (Table S3, Figs. 3 and S6). These findings support our deductions from the TEM and NanoSIMS analyses that the ferrihydrite nanoparticles are associated with an OM-Si matrix or coating.

The molecular structure around Fe in the colloids was further characterized using Fe K-edge EXAFS (Fig. 4). Snowmelt and baseflow colloid samples were selected for additional analyses, including LC-LS fitting (Table S4; Figs S7–8) and shell-by-shell fitting (Fig. 4; Table S5). Both samples contained a mixture of Fe(II) and Fe(III), as demonstrated in the derivative Fe K-edge XANES spectra (Fig. 4). Yet the snowmelt colloid (0.02–0.22 μm) sample had a higher absolute Fe(II) content whereas the baseflow colloid sample had a higher Fe(III) content, in accordance with measured bulk Fe(II) and Fe(III) colloid concentrations (Table S2).

EXAFS spectra from the baseflow colloids visibly resemble the spectra of ferrihydrite (Fig 4, middle and bottom panels). Linear combination-least squares (LC-LS) fitting was employed to identify major Fe phases present and to compare/contrast the baseflow and

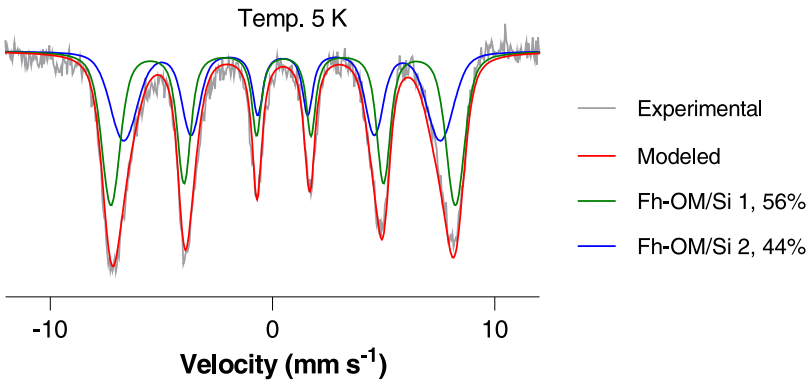

Fig 3. Mössbauer spectrum (at 5 K) of Fe-rich colloids collected at 180 cm depth under baseflow conditions (Sept 16–17, 2021), including experimental and modeled spectra (goodness of fit, χ^2=1.8). Ferrihydrite (Fh) associated with varying proportions of organic matter (OM) and/or Si (Fh-OM/Si) were the best fit components (increasing OM/Si loading from Fh-OM/Si 1 to 2).

snowmelt colloids. We found that four distinct model spectra were required for acceptable fits: ferrihydrite, ferrihydrite coated with OM, and complexes of Fe(II) and Fe(III) with OM (Table S4; Figs. S7–8). Superiority of ferrihydrite is illustrated in the Fourier Transform (Fig. 4) with first and second neighbor peaks at ~1.5 and ~2.7 Å, respectively. Fit to the snowmelt colloids was poorer at 8 $Å^{-1}$, indicating that none of the reference compounds (Table S6) provide a perfect match to the natural samples (as expected). Nevertheless, these results clearly support the conclusion that multiple Fe-bearing species are present, and moreover that both ferrihydrite and Fe-OM complexes are present in the colloidal assemblages. Ferrihydrite increased in relative abundance from 21% (snowmelt) to 43% (baseflow) of total Fe species as the hydrological site conditions changed from wet to dry (Table S4). The relative abundance of Fe(II)-OM complexes changed in the opposite direction, dropping from 36% to 11% of total Fe over this same time frame. The snowmelt colloids are evidently more reduced (*e.g.*, higher relative abundance of Fe(II)) than the baseflow colloids. These observations demonstrate a variable composition of the colloid assemblages, in response to changing aqueous chemical and hydrological conditions.

3.3. Quantitative molecular structure around Fe

Shell-by-shell fitting of the Fe EXAFS spectra was performed to quantify the molecular environment around Fe in the colloid assemblages (Fig. 4), as well as to supplement the results of the LC-LS fitting, particularly of the snowmelt colloids. In all samples, the fits indicated Fe–O distances of -1.95 and ~2.08 Å, and Fe–Fe distances of ~3.07 Å, which are typical for Fe oxyhydroxide minerals such as ferrihydrite (Table S5). Fe(II) or Fe(III) coordinated to organic compounds, *e.g.*, through carboxylate or phenolic functional groups (Yu et al., 2015; Daugherty et al., 2017), may also be present. Fits were attempted with C neighbors being present at *ca* 2.8 Å, which would indicate bidentate coordination of Fe by carboxylate groups. This shell improved the fits substantially, but the fitted parameters had relatively high uncertainty (likely due to the presence of C neighbors at multiple distances and overlap with the EXAFS from Fe neighbors) and are not included in the presented fits. A second Fe–Fe pair distinguished by a 2.87 Å interatomic distance (Table S5; Fig. S9) may be attributed to a tetrahedral Fe(II) coordination environment (Skomurski et al., 2010). S neighbors at 2.27 Å, which were essential to fit the snowmelt EXAFS (Fig. S9), are characteristic of Fe–S bond distances in sulfides. Yet, neither FeS or FeS_2 were detected in Fe EXAFS LC-LS (Table S4) or Mössbauer analyses (Fig. 3). Therefore, we infer that S is a minor constituent of ferrihydrite (likely a result of superficial sulfidation). The presence of S(-II) and Fe (II) in the snowmelt colloids is consistent with the conclusion above that they are more chemically reduced compared to the baseflow colloids.

4. Discussion

4.1. Molecular structure and mechanisms of persistence of Fe-based colloids

Ferrihydrite is a widespread Fe oxyhydroxide (Schwertmann and Taylor, 1989) in soils, sediments, rivers and lakes (Kennedy et al., 2004; Jambor and Dutrizac, 1998). Its abundance may be attributed to its rapid precipitation kinetics – it is usually the first solid Fe oxyhydroxide phase to form upon oxidation of dissolved ferrous iron (Guo and Barnard, 2013). Individual ferrihydrite particles are typically several nm in size, aggregated, (Schwertmann and Taylor, 1989) and reactive, readily transforming into other Fe oxyhydroxides (Thomasarrigo et al., 2019; Schwertmann and Taylor, 1989). Few reports exist on stable colloidal ferrihydrite particles in natural settings, particularly under reducing/sulfidic conditions (Homoky et al., 2021; Gomez-Gonzalez et al., 2016). In this study, we found that despite anoxic conditions (dissolved oxygen < 0.08 mg L^{-1}) and the presence of dissolved Fe(II), a significant portion of the colloidal Fe occurred in its oxidized form as ferrihydrite, as supported by SAED (Fig. 2), Mössbauer (Fig. 3) and Fe-EXAFS measurements (Fig. 4, Table S4, S5, Fig. S7). To the best of our knowledge, this study is the first to identify natural mobile ferrihydrite-based colloids that persist in anoxic waters.

The roles that colloids play in biogeochemical cycling, and in the regulation of nutrient, contaminant, and OM availability and transport, depend on the structures and compositions of the phases that co-occur in the colloids and on how they behave in ensemble. In this study, ferrihydrite is coated with Si and OM and the ferrihydrite cores appear to be intimately associated with organic matter complexed to Fe(II)/Fe(III). Adsorption or coprecipitation of Si and OM are evident. Moreover, despite excess aqueous Fe(II) at our sampling depth (Table S2), no Fe(II)-catalyzed transformation of our ferrihydrite-based colloids to secondary minerals such as goethite, magnetite, and lepidocrocite (Qafoku et al., 2020; Hansel et al., 2005; Cornell and Giovanoli, 1985; Schwertmann and Taylor, 1989) was observed (Figs. 3 and S6). The presence of coatings is significant because they are expected to kinetically or chemically stabilize the underlying nano-sized (~30 nm) ferrihydrite particles. Previous studies have reported that ferrihydrite transformation is inhibited in the presence of organic/inorganic compounds and SiO_4^{4-} (Kaegi et al., 2010; Giannetta et al., 2020; Zhou et al., 2018), as well as PO_4^{3-} (Kraal et al., 2022). In the case of Si, reductive transformation of Si-ferrihydrite coprecipitates was significantly retarded at solid phase Si/Fe molar ratios above 0.18 (Schulz et al., 2022; Kaegi et al., 2010; Cismasu et al., 2013). Similarly, for organic compounds C/Fe molar ratios above 1.6 have been reported to completely inhibit abiotic OM-ferrihydrite coprecipitate transformation (Chen et al., 2015), though a different study found that ratios above 1.8 can enhance

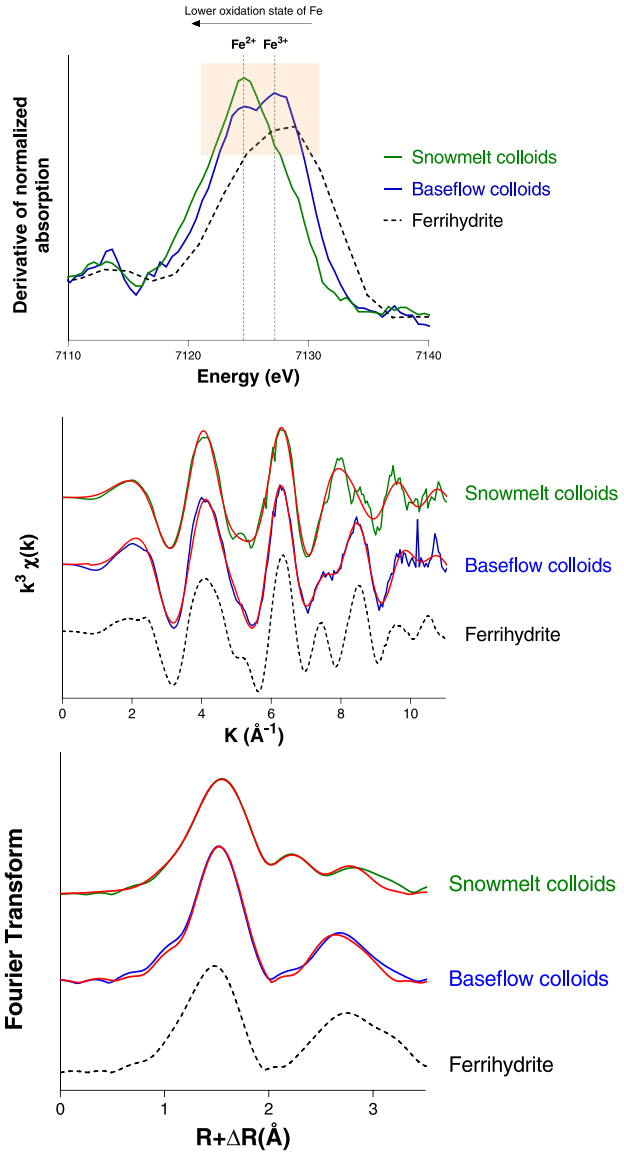

Fig 4. Fe *K*-edge X-ray absorption near edge structure (XANES) and extended X-ray absorption fine structure (EXAFS) spectra of Fe-rich colloids collected at 180 cm depth during baseflow (July 19) and snowmelt (June 15) 2021, as well as ferrihydrite. Top panel: 1st derivative XANES spectra; Middle panel: EXAFS spectra; Bottom panel: Fourier transform magnitude. Red lines correspond to the shell-by-shell fitting results (parameters listed in Table S5).

the biotic transformation pathway (Shimizu et al., 2013). In comparison, we observed high relative molar ratios of C/Fe (12.8) and Si/Fe (1.0) (Jones et al., 2009). This implies organic molecules of comparable size are associated with the ferrihydrite nanoparticles, that are either coprecipitated and/or adsorbed (Yang et al., 2017). The superior C/Fe ratios of our natural colloids compared to laboratory synthesized analogues (C/Fe<2.5) provide an explanation for the stability of these natural colloids against reductive transformation. Factors that favor delay/inhibition of transformation likely include: 1) high OM/Si loading and resulting coverage of the ferrihydrite surface (Schulz et al., 2022; Giannetta et al., 2020; Cismasu et al., 2013; Thomasarrigo et al., 2018); 2) the presence of OM-Fe(II) complexes in solution, which can bond and stabilize ferrihydrite (Pédrot et al., 2011), and 3) surface organic functional groups – particularly the extent and type of associated ligands (Zhou et al., 2018). For the latter, carboxylic acids play a key role in ferrihydrite transformation, with the number of bound *versus* free carboxyl groups regulating surface reactivity (Thomasarrigo et al., 2019). Ultimately, in this study we ascribe colloid persistence under anoxic/reducing conditions to the passivating effect conferred by OM and Si coatings.

Though no Fe(II)-catalyzed transformation of ferrihydrite was observed, our results do reveal that Fe(II) is part of the colloidal assemblage, likely as Fe(II) complexed by the OM-matrix (as inferred from the Fe-EXAFS LC-LS fitting) and/or embedded in the ferrihydrite structure (as inferred from the Fe-EXAFS shell-by-shell fitting). Previous studies on the biotransformation of ferrihydrite have reported an intermediate Fe(II)-enriched ferrihydrite in which Fe(II) is incorporated into the mineral structure with minimal phase change (Zachara et al., 2007). Thus, we conclude that ferrihydrite-based colloids in this study are coated by Si or encapsulated in an OM matrix that inhibits redox-triggered transformations under conditions where pristine ferrihydrite would not prevail.

Ferrihydrite-OM-Si associations in the colloids may serve a dual purpose, which extends their passivating properties to offer protection against OM degradation. This can be attributed to the strong OM-mineral interaction and/or to the formation of inaccessible OM domains (Mikutta et al., 2006; Eusterhues et al., 2014; Baldock and Skjemstad, 2000). The incorporation of Si as part of the OM-Si matrix may offer enhanced protection against biological attack (Tamrat et al., 2019). Because OM is a dominant component of the colloids, their role in OM preservation, as well as OM transport is expected to be important.

4.2. *Watershed-scale implications of Fe-based colloid persistence*

The "dissolved" Fe pool (*i.e.*, Fe that passes through *a* <0.45 μm membrane in ground- and surface water investigations) has long been recognized to contain a mixture of soluble Fe(II), and OM-complexed and colloidal Fe (Perdue et al., 1976; Koenings, 1976). The colloidal contribution varies substantially in terrestrial and aquatic systems; bulk Fe colloids of unknown phase identity and composition contributed between 17% and 99% of the total Fe in porewaters of marine sediments (20–200 nm sized colloids) (Homoky et al., 2021), and between 30% and 50% in porewaters of peat soils (> 10 kDa sized colloids) (Pokrovsky et al., 2005). In this study, between 48% and 72% of the porewater Fe at 180 cm depth was present as colloidal ferrihydrite-nanoparticles (20–220 nm; Table S2).

The presence of variable redox zones along groundwater flow paths is generally thought to be a barrier to advective transport of redox-sensitive Fe minerals, such as ferrihydrite, which undergo rapid reductive/oxidative dissolution or precipitation/partitioning to solid phase when appearing as compositionally pure materials (Adhikari et al., 2019; Noël et al., 2017). However, while Fe transport could in principle occur through a series of colloid precipitation and dissolution steps along the groundwater flowpath, *i.e.*, as redox transitions occur, this study suggests that a different mechanism prevails. Rather, we show that mobile ferrihydrite-based colloids persist in anoxic soil water, which implies that they can be transported through reduced zones containing abundant dissolved Fe(II) and discharged into surface waters. Given the considerable colloidal mass (up to 30 mg L^{-1} Fe colloids) in Slate River floodplain soil water, especially during snowmelt (Table S2), it is reasonable to conclude that colloid-borne Fe and OM may contribute significantly to element loading in Slate River (where the concentration of Fe is 10–100 μg L^{-1}). This conclusion emphasizes the need to improve colloid process representations (Flury and Qiu, 2008; Johnson et al., 1996) in watershed reactive transport models (Steefel et al., 2015).

4.3. *Seasonal variability of Fe-based colloid composition*

Our colloids demonstrated seasonal compositional variability, *i.e.*, the baseflow colloids were more oxidized compared to the snowmelt colloids (Tables S4–5 and Figs. 3-4 and S7). LC-LS fitting of the Fe-EXAFS spectra showed that the contribution of ferrihydrite to the

colloidal assemblage was 41% during snowmelt, which increased to >60% under baseflow conditions. In comparison, the fraction of Fe(II) decreased from 36% to 11% following the spring snowmelt, in apparent response to intrusion of dissolved oxygen in July (Table S2 and S4). Oxidation of Fe(II) is likely a primary driving force for the compositional variations witnessed in the baseflow colloids. Thus, the decrease in OM and Fe(II) in colloids collected under baseflow conditions can be attributed to decreasing abundance of Fe(II)-OM complexes. This conclusion is consistent with previous riverine observations on the transport of Fe as OM-associated colloids from soils during spring snowmelt (Olshansky et al., 2018). Thus, it appears that seasonal hydrological events such as rainfall, flooding, and snowmelt, can play important roles in regulating colloid concentrations and composition in floodplains.

5. Conclusions

These findings confirm the presence of mobile ferrihydrite-based, OM-associated colloids in anoxic groundwater of a montane riparian floodplain. We provide direct observational evidence in support of the riverine-based work of Olshansky (2018), which concluded that soil-derived Fe-OM colloids were important sources of Fe loading in mountain streams. The fact that Fe(II) and S are incorporated in a ferrihydrite-based colloidal assemblage, under anoxic conditions with excess dissolved Fe(II), implies that Fe(III) in ferrihydrite is passivated against reductive dissolution. This stability is attributed to the presence of Si and OM coatings. The persistence of these nominally redox-active colloids under both anoxic and oxic conditions sheds new light on their ability to transport Fe, OM, and nutrients across terrestrial-aquatic interfaces.

Declaration of Competing Interest

The authors declare that they have no known competing financial interests or personal relationships that could have appeared to influence the work reported in this paper.

Data availability

Data will be made available on request.

Acknowledgments

Funding was provided by the U.S. Department of Energy (DOE) office of Biological and Environmental Research (BER), Environmental System Sciences Division, through its support of the SLAC Floodplain Hydro-Biogeochemistry Science Focus Area (SFA) under Contract No. DE-AC02–76SF00515. SSRL and SLAC are supported by the U.S. Department of Energy, Office of Science, Office of Basic Energy Sciences. The technical staff at SSRL are gratefully acknowledged for their support of the X-ray absorption measurements. We further acknowledge the use and support of the Stanford-SLAC Cryo-EM Facilities, which is supported by the National Institutes of Health Common Fund Transformative High-Resolution Cryo-Electron Microscopy program (U24 GM129541). W.Z is funded by the Stanford Interdisciplinary Graduate Fellowship program. A portion of this research was performed on a project award (10.46936/lser.proj.2021.51929/60000375) from the Environmental Molecular Sciences Laboratory, a DOE Office of Science User Facility sponsored by the Biological and Environmental Research program under Contract No. DE-AC05–76RL01830.

Supplementary materials

Supplementary material associated with this article can be found, in the online version, at doi:10.1016/j.watres.2023.119990.

References

Boye, M., et al., 2010. Significant portion of dissolved organic Fe complexes in fact is Fe colloids. Mar. Chem. 122, 20–27.
Homoky, W.B., et al., 2021. Iron colloids dominate sedimentary supply to the ocean interior. Proc. Natl. Acad. Sci. U. S. A. 118.
Liao, P., et al., 2020. Formation and transport of Cr(III)-NOM-Fe colloids upon reaction of Cr(VI) with NOM-Fe(II) colloids at anoxic-oxic interfaces. Environ. Sci. Technol. 54, 4256–4266.
Thompson, A., Chadwick, O.A., Boman, S., Chorover, J., 2006a. Colloid mobilization during soil iron redox oscillations. Environ. Sci. Technol. 40, 5743–5749.
Yan, J., Lazouskaya, V., Jin, Y., 2016. Soil colloid release affected by dissolved organic matter and redox conditions. Vadose Zo. J. 15, 1–10.
Löv, Å., et al., 2018. Particle- and colloid-facilitated Pb transport in four historically contaminated soils - Speciation and effect of irrigation intensity. Appl. Geochem. 96, 327–338.
Henderson, R., et al., 2012. Anoxia-induced release of colloid- and nanoparticle-bound phosphorus in grassland soils. Environ. Sci. Technol. 46, 11727–11734.
Liao, P., et al., 2017. Formation, aggregation, and deposition dynamics of NOM-iron colloids at anoxic-oxic interfaces. Environ. Sci. Technol. 51, 12235–12245.
Pokrovsky, O.S., Schott, J., 2002. Iron colloids/organic matter associated transport of major and trace elements in small boreal rivers and their estuaries (NW Russia). Chem. Geol. 190, 141–179.
Mylon, S.E., Chen, K.L., Elimelech, M., 2004. Influence of natural organic matter and ionic composition on the kinetics and structure of hematite colloid aggregation: implications to iron depletion in estuaries. Langmuir 20, 9000–9006.
Olshansky, Y., White, A.M., Moravec, B.G., McIntosh, J., Chorover, J., 2018. Subsurface pore water contributions to stream concentration-discharge relations across a snowmelt hydrograph. Front. Earth Sci. 6, 1–18.
Liao, P., Yuan, S., Wang, D., 2016. Impact of redox reactions on colloid transport in saturated porous media: an example of ferrihydrite colloids transport in the presence of sulfide. Environ. Sci. Technol. 50, 10968–10977.
He, L., et al., 2019. Elucidating the role of sulfide on the stability of ferrihydrite colloids under anoxic conditions. Environ. Sci. Technol. 53, 4173–4184.
Noël, V., et al., 2020. FeS colloids-formation and mobilization pathways in natural waters. Environ. Sci. Nano 7, 2102–2116.
Thomasarrigo, L.K., Bouchet, S., Kaegi, R., Kretzschmar, R., 2020. Organic matter influences transformation products of ferrihydrite exposed to sulfide. Environ. Sci. Nano 7, 3405–3418.
Sharma, P., Ofner, J., Kappler, A., 2010. Formation of binary and ternary colloids and dissolved complexes of organic matter, Fe and As. Environ. Sci. Technol. 44, 4479–4485.
Schulz, K., Thomasarrigo, L.K., Kaegi, R., Kretzschmar, R., 2022. Stabilization of ferrihydrite and lepidocrocite by silicate during fe(II)-catalyzed mineral transformation: impact on particle morphology and silicate distribution. Environ. Sci. Technol. 56, 5929–5938.
Kaegi, R., Voegelin, A., Folini, D., Hug, S.J., 2010. Effect of phosphate, silicate, and Ca on the morphology, structure and elemental composition of Fe(III)-precipitates formed in aerated Fe(II) and As(III) containing water. Geochim. Cosmochim. Acta 74, 5798–5816.
Jakobsen, R., Postma, D., 1999. Redox zoning, rates of sulfate reduction and interactions with Fe-reduction and methanogenesis in a shallow sandy aquifer, Romo, Denmark. Geochim. Cosmochim. Acta 63, 137–151.
Hassellöv, M., von der Kammer, F., 2008. Iron oxides as geochemical nanovectors for metal transport in soil-river systems. Elements 4, 401–406.
Qafoku, O., et al., 2020. Nanoscale observations of Fe(ii)-induced ferrihydrite transformation. Environ. Sci. Nano 7, 2953–2967.
Thompson, A., Chadwick, O.A., Rancourt, D.G., Chorover, J., 2006b. Iron-oxide crystallinity increases during soil redox oscillations. Geochim. Cosmochim. Acta 70, 1710–1727.
Thomasarrigo, L.K., Kaegi, R., Kretzschmar, R., 2019. Ferrihydrite growth and transformation in the presence of ferrous iron and model organic ligands. Environ. Sci. Technol. 53, 13636–13647.
Hansel, C.M., Benner, S.G., Fendorf, S., 2005. Competing Fe (II)-induced mineralization pathways of ferrihydrite. Environ. Sci. Technol. 39, 7147–7153.
Cornell, R.M., Giovanoli, R., 1985. Effect of solution conditions on the proportion and morphology of goethite formed from ferrihydrite. Clays Clay Miner. 33, 424–432.
Lapworth, D.J., Stolpe, B., Williams, P.J., Gooddy, D.C., Lead, J.R., 2013. Characterization of suboxic groundwater colloids using a multi- method approach. Environ. Sci. Technol. 47, 2554–2561.
Moens, C., Montalvo, D., Smolders, E., 2021. The concentration and size distribution of iron-rich colloids in pore waters are related to soil organic matter content and pore water calcium concentration. Eur. J. Soil Sci. 72, 2199–2214.
Stolpe, B., Guo, L., Shiller, A.M., 2013. Binding and transport of rare earth elements by organic and iron-rich nanocolloids in alaskan rivers, as revealed by field-flow fractionation and ICP-MS. Geochim. Cosmochim. Acta 106, 446–462.
Jones, A.M., Collins, R.N., Rose, J., Waite, T.D., 2009. The effect of silica and natural organic matter on the Fe(II)-catalysed transformation and reactivity of Fe(III) minerals. Geochim. Cosmochim. Acta 73, 4409–4422.
Kukkadapu, R.K., Zachara, J.M., Fredrickson, J.K., Kennedy, D.W., 2004. Biotransformation of two-line silica-ferrihydrite by a dissimilatory Fe(III)-reducing bacterium: formation of carbonate green rust in the presence of phosphate. Geochim. Cosmochim. Acta 68, 2799–2814.
Li, Q., et al., 2019. Formation and stability of NOM-Mn(III) colloids in aquatic environments. Water Res. 149, 190–201.

Rod, K.A., et al., 2020. Dispersible colloid facilitated release of organic carbon from two contrasting riparian sediments. Front. Water 2, 1–8.
Xia, B., Qiu, H., Knorr, K.H., Blodau, C., Qiu, R., 2018. Occurrence and fate of colloids and colloid-associated metals in a mining-impacted agricultural soil upon prolonged flooding. J. Hazard. Mater. 348, 56–66.
Viollier, E., Inglett, P.W., Hunter, K., Roychoudhury, A.N., Van Cappellen, P., 2000. The Ferrozine method revisted. Appl. Geochem. 15, 785–790.
Stookey, L.L., 1970. Ferrozine-A new spectrophotometric reagent for iron. Anal. Chem. 42, 779–781.
Peretyazhko, T.S., et al., 2012. Pertechnetate (TcO4-) reduction by reactive ferrous iron forms in naturally anoxic, redox transition zone sediments from the Hanford Site, USA. Geochim. Cosmochim. Acta 92, 48–66.
Ravel, B., Newville, M., 2005. ATHENA, ARTEMIS, HEPHAESTUS: data analysis for X-ray absorption spectroscopy using IFEFFIT. J. Synchrotron Radiat. 12, 537–541.
Ostergren, J.D., Brown, G.E., Parks, G.A., Tingle, T.N., 1999. Quantitative speciation of lead in selected mine tailings from Leadville. CO. Environ. Sci. Technol. 33, 1627–1636.
Cancès, B., et al., 2005. XAS evidence of As(V) association with iron oxyhydroxides in a contaminated soil at a former arsenical pesticide processing plant. Environ. Sci. Technol. 39, 9398–9405.
Ankudinov, A., Ravel, B., 1998. Real-space multiple-scattering calculation and interpretation of x-ray-absorption near-edge structure. Phys. Rev. B Condens. Matter Mater. Phys. 58, 7565–7576.
Liu, Y.T., Hesterberg, D., 2011. Phosphate bonding on noncrystalline Al/Fe-hydroxide coprecipitates. Environ. Sci. Technol. 45, 6283–6289.
Trostle, K.D., et al., 2016. Colloids and organic matter complexation control trace metal concentration-discharge relationships in Marshall Gulch stream waters. Water Resour. Res. 5, 2–2.
Dewey, C., Bargar, J.R., Fendorf, S., 2021. Porewater Lead concentrations limited by particulate organic matter coupled with ephemeral iron(III) and sulfide phases during redox cycles within contaminated floodplain soils. Environ. Sci. Technol. 55, 5878–5886.
Adusei-Gyamfi, J., Ouddane, B., Rietveld, L., Cornard, J.P., Criquet, J., 2019. Natural organic matter-cations complexation and its impact on water treatment: a critical review. Water Res. 160, 130–147.
Janney, D.E., Cowley, J.M., Buseck, P.R., 2000. Transmission electron microscopy of synthetic 2- and 6-line ferrihydrite. Clays Clay Miner. 48, 111–119.
Dardenne, K., et al., 2002. Low temperature XAFS investigation on the Lutetium binding changes during the 2-line ferrihydrite alteration process. Environ. Sci. Technol. 36, 5092–5099.
Chen, C., Kukkadapu, R., Sparks, D.L., 2015. Influence of coprecipitated organic matter on Fe2+(aq)-catalyzed transformation of ferrihydrite: implications for carbon dynamics. Environ. Sci. Technol. 49, 10927–10936.
Eusterhues, K., et al., 2008. Characterization of ferrihydrite-soil organic matter coprecipitates by X-ray diffraction and Mössbauer spectroscopy. Environ. Sci. Technol. 42, 7891–7897.
Murad, E., Cashion, J., 2004. Data analysis and interpretation. Mossbauer Spectrosc. Environ. Mater. 88–144.
Yu, C., et al., 2015. Iron behavior in a northern estuary: large pools of non-sulfidized Fe (II) associated with organic matter. Chem. Geol. 413, 73–85.
Daugherty, E.E., Gilbert, B., Nico, P.S., Borch, T., 2017. Complexation and redox buffering of iron(II) by dissolved organic matter. Environ. Sci. Technol. 51, 11096–11104.
Skomurski, F.N., Kerisit, S., Rosso, K.M., 2010. Structure, charge distribution, and electron hopping dynamics in magnetite (Fe3O4) (100) surfaces from first principles. Geochim. Cosmochim. Acta 74, 4234–4248.
Schwertmann, U., Taylor, R.M., 1989. Iron oxides. Miner. Soil Environ. 379–438.
Kennedy, C.B., Scott, S.D., Ferris, F.G., 2004. Hydrothermal phase stabilization of 2-line ferrihydrite by bacteria. Chem. Geol. 212, 269–277.
Jambor, J.L., Dutrizac, J.E., 1998. Occurrence and constitution of natural and synthetic ferrihydrite, a widespread iron oxyhydroxide. Chem. Rev. 98, 2549–2585.
Guo, H., Barnard, A.S., 2013. Naturally occurring iron oxide nanoparticles: morphology, surface chemistry and environmental stability. J. Mater. Chem. A 1, 27–42.
Gomez-Gonzalez, M.A., et al., 2016. Colloidal mobilization of arsenic from mining-affected soils by surface runoff. Chemosphere 144, 1123–1131.
Pédrot, M., Boudec, A.Le, Davranche, M., Dia, A., Henin, O., 2011. How does organic matter constrain the nature, size and availability of Fe nanoparticles for biological reduction? J. Colloid Interface Sci. 359, 75–85.
Giannetta, B., et al., 2020. Fe(II)-catalyzed transformation of Fe (oxyhydr)oxides across organic matter fractions in organically amended soils. Sci. Total Environ. 748, 141125.
Zhou, Z., et al., 2018. Fe(II)-catalyzed transformation of organic matter-ferrihydrite coprecipitates: a closer look using Fe isotopes. Environ. Sci. Technol. 52, 11142–11150.
Kraal, P., van Genuchten, C.M., Behrends, T., 2022. Phosphate coprecipitation affects reactivity of iron (oxyhydr)oxides towards dissolved iron and sulfide. Geochim. Cosmochim. Acta 321, 311–328.
Cismasu, A.C., Levard, C., Michel, F.M., Brown, G.E., 2013. Properties of impurity-bearing ferrihydrite II: insights into the surface structure and composition of pure, Al- and Si-bearing ferrihydrite from Zn(II) sorption experiments and Zn K-edge X-ray absorption spectroscopy. Geochim. Cosmochim. Acta 119, 46–60.
Shimizu, M., et al., 2013. Dissimilatory reduction and transformation of ferrihydrite-humic acid coprecipitates. Environ. Sci. Technol. 47, 13375–13384.
Yang, Y., Lohwacharin, J., Takizawa, S., 2017. Analysis of adsorption processes of dissolved organic matter (DOM) on ferrihydrite using surrogate organic compounds. Environ. Sci. Pollut. Res. 24, 21867–21876.
Thomasarrigo, L.K., Byrne, J.M., Kappler, A., Kretzschmar, R., 2018. Impact of organic matter on iron(II)-catalyzed mineral transformations in ferrihydrite-organic matter coprecipitates. Environ. Sci. Technol. 52, 12316–12326.
Zachara, J.M., et al., 2007. Reduction of pertechnetate [Tc(VII)] by aqueous Fe(II) and the nature of solid phase redox products. Geochim. Cosmochim. Acta 71, 2137–2157.
Mikutta, R., Kleber, M., Torn, M.S., Jahn, R., 2006. Stabilization of soil organic matter: association with minerals or chemical recalcitrance? Biogeochemistry 77, 25–56.
Eusterhues, K., Neidhardt, J., Hädrich, A., Küsel, K., Totsche, K.U., 2014. Biodegradation of ferrihydrite-associated organic matter. Biogeochemistry 119, 45–50.
Baldock, J.A., Skjemstad, J.O., 2000. Role of the soil matrix and minerals in protecting natural organic materials against biological attack. Org. Geochem. 31, 697–710.
Tamrat, W.Z., et al., 2019. Soil organo-mineral associations formed by co-precipitation of Fe, Si and Al in presence of organic ligands. Geochim. Cosmochim. Acta 260, 15–28.
Perdue, E.M., Beck, K.C., Helmut Reuter, J., 1976. Organic complexes of iron and aluminium in natural waters. Nature 260, 418–420.
Koenings, J.P., 1976. In situ experiments on the dissolved and colloidal state of iron in an acid bog lake. Limnol. Oceanogr. 21, 674–683.
Pokrovsky, O.S., Dupré, B., Schott, J., 2005. Fe-Al-organic colloids control of trace elements in peat soil solutions: results of ultrafiltration and dialysis. Aquat. Geochem. 11, 241–278.
Adhikari, D., et al., 2019. Formation and redox reactivity of ferrihydrite-organic carbon-calcium co-precipitates. Geochim. Cosmochim. Acta 244, 86–98.
Noël, V., et al., 2017. Understanding controls on redox processes in floodplain sediments of the upper colorado river basin. Sci. Total Environ. 663–675, 603–604.
Flury, M., Qiu, H., 2008. Modeling colloid-facilitated contaminant transport in the Vadose Zone. Vadose Zone J. 7, 682–697.
Johnson, P.R., Sun, N., Elimelech, M., 1996. Colloid transport in geochemically heterogeneous porous media: modeling and measurements. Environ. Sci. Technol. 30, 3284–3293.
Steefel, C.I., et al., 2015. Reactive transport codes for subsurface environmental simulation. Comput. Geosci. 19, 445–478.